Supplement of Atmos. Chem. Phys., 23, 13125–13141, 2023
https://doi.org/10.5194/acp-23-13125-2023-supplement

Atmospheric Chemistry and Physics
Open Access
EGU

Supplement of

Global observations of aerosol indirect effects from marine liquid clouds

Casey J. Wall et al.

Correspondence to: Casey J. Wall (c.j.wall@geo.uio.no)

Supplementary Figures

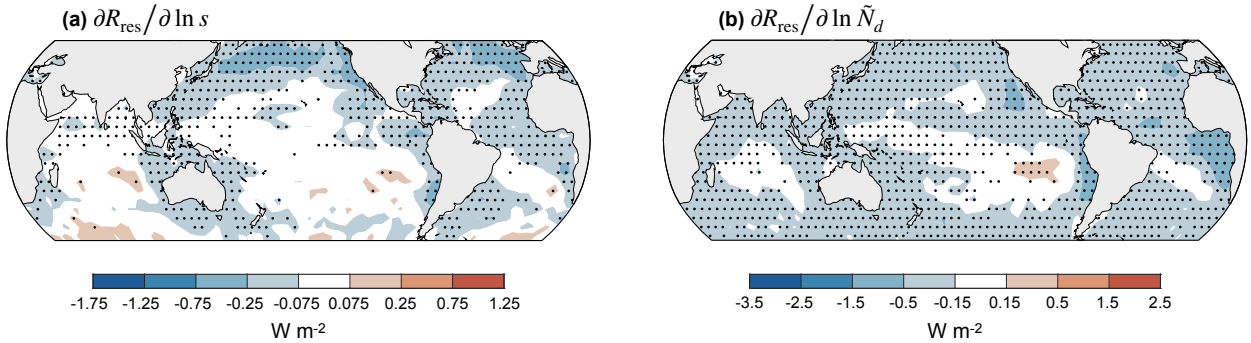

Fig. S1 Relationships between the residual of the R decomposition (R_{res}) and local anomalies of two indicators of cloud-base CCN concentration. The CCN indicators include sulfate aerosol mass concentration at 910 hPa (s) and cloud-droplet number concentration from pixels with the largest 10% cloud optical thickness ($\widetilde{N}_d$). Linear regression coefficients are plotted for (a) $\partial R_{\mathrm{res}}/\partial \ln s$ and (b) $\partial R_{\mathrm{res}}/\partial \ln \widetilde{N}_d$. Stippling indicates regression coefficients that are significantly different from zero with the false discovery rate limited to 0.1 (Wilks, 2016). The averages of $\partial R_{\mathrm{res}}/\partial \ln s$ and $\partial R_{\mathrm{res}}/\partial \ln \widetilde{N}_d$ over ocean between 55°S and 55°N are -0.08 ± 0.01 W m^{-2} and -0.26 ± 0.01 W m^{-2}, respectively (95% CIs). Cloud radiative effects are computed with only fully cloud-covered pixels included in the cloud histograms (MODIS$_{\mathrm{CLD}}$). Note that the contour values are one order of magnitude smaller than those in Fig. 2 of the main text.

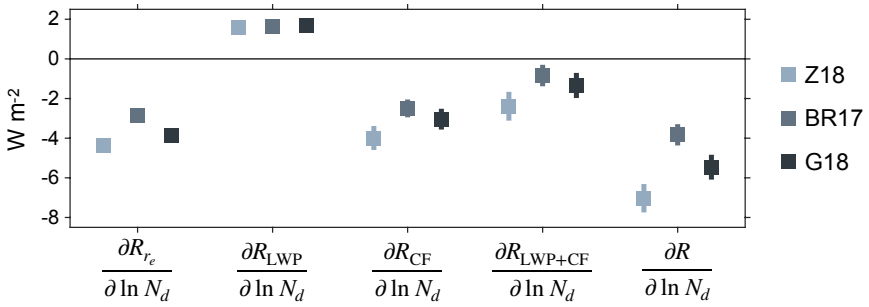

Fig. S2 Sensitivity test showing how the spatial average of $\partial R/\partial \ln N_d$ depends on the retrieval method for N_d. The Z18, BR17, and G18 cases retrieve N_d using filtering methods recommended by Zhu et al. (2018), Bennartz and Rausch (2017), and Grosvenor et al. (2018), respectively. These filtering methods select N_d in different subsets of liquid-cloud pixels. The Z18 case is presented in the main text, where it is referred to as $\widetilde{N}_d$. Squares show mean values, and vertical lines show 95% CIs. Cloud radiative effects are computed with only fully cloud-covered pixels included in the cloud histograms ($\mathrm{MODIS_{CLD}}$).

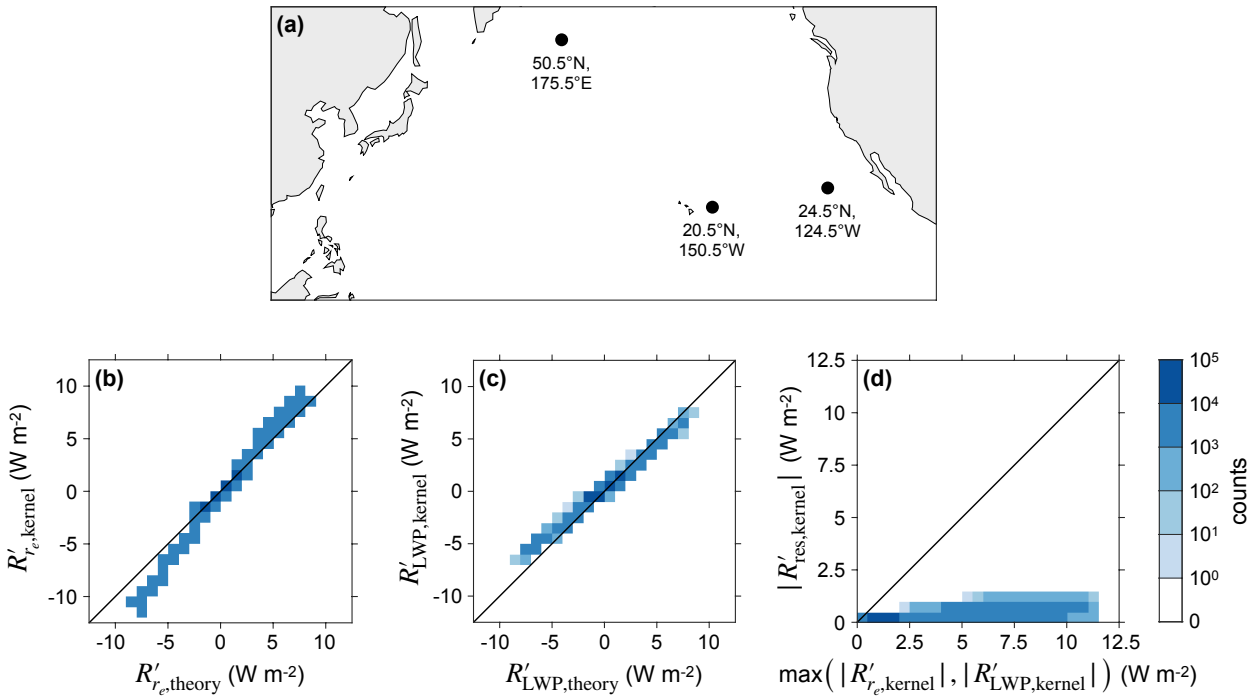

Fig. S3 Validation of the R' decomposition using synthetic-data test cases. (a) Locations of the $1° \times 1°$ grid boxes used in the test cases. The center of the grid box is labeled on the map. (b) Joint histogram showing the kernel-based estimate of R'_{r_e} plotted as a function of the theoretical estimate of R'_{r_e}. Each data point in the histogram represents one test case. (c) Similar to (b), but for R'_{LWP}. (d) Joint histogram showing the magnitude of the residual of the decomposition, $|R'_{\mathrm{res}}|$, plotted as function of the maximum of $|R'_{r_e}|$ and $|R'_{\mathrm{LWP}}|$. Values in (d) are computed using the kernel method. The color scale is logarithmic, and the bin spacing is 1 W m^{-2} in (b-c) and 0.5 W m^{-2} in (d).

Supplementary Tables

Table S1 List of GCMs used in the study. CMIP6 output is used to compute $\Delta \ln s$, and CMIP5 and AeroCom output is used to compute the GCM estimates of ERF_{aci} in Fig. 5 of the main text. CMIP6 and CMIP5 models are listed according to their Source ID on the CMIP online archives (https://esgf-node.llnl.gov/projects/cmip6/; https://esgf-node.llnl.gov/projects/cmip5/), and AeroCom models are listed according to the naming convention of Gryspeerdt et al. (2020).

CMIP6 Models	CMIP5 Models	AeroCom Models
BCC-ESM1	CanESM2	ECHAM6-HAM2.2
CESM2	HadGEM2-A	HadGEM3-UKCA
CESM2-FV2	IPSL-CM5A-LR	CAM5.3
CESM2-WACCM	MIROC5	CAM5.3-MG2
CESM2-WACCM-FV2	MRI-CGCM3	CAM5.3-CLUBB
CNRM-ESM2-1		CAM5.3-CLUBB-MG2
EC-Earth3-AerChem		SPRINTARS
GISS-E2-1-G		SPRINTARS-KK
GISS-E2-1-H		UKESM1-A
HadGEM3-GC31-LL		
IPSL-CM5A2-INCA		
IPSL-CM6A-LR-INCA		
KIOST-ESM		
MIROC6		
MIROC-ES2L		
MPI-ESM-1-2-HAM		
MRI-ESM2-0		
NorESM2-LM		
NorESM2-MM		
UKESM1-0-LL		

Table S2 Parameters for estimating SW ERF_{aci} from liquid clouds following the method of Bellouin et al. (2020; hereafter B20). The table includes the parameter, its notation in B20, the original 66% CI that B20 estimated for the global mean, and the revised 66% CI that we estimate for the mean over ocean between 55°S and 55°N.

Parameter	Notation in B20	Original 66% CI	Revised 66% CI
present-day aerosol optical thickness	τ_a	0.13 to 0.17	0.11 to 0.15
change in aerosol optical thickness between preindustrial and present day	$\Delta\tau_a$	0.02 to 0.04	0.015 to 0.031
$\frac{\partial R}{\partial \ln N_d}$ (W m^{-2})	S_N	-27 to -26	-30 to -29
$\frac{\partial R}{\partial \ln \mathrm{LWP}}$ (W m^{-2})	$S_{\mathcal{L},N}$*	-56 to -54**	-75 to -73**
$\frac{\partial R}{\partial C_{\mathrm{tot}}}$ (W m^{-2})	$S_{C,N}$*	-153 to -91**	-184 to -111**
$\frac{\partial \ln N_d}{\partial \ln \tau_a}$	$\beta_{\ln N - \ln \tau}$	0.3 to 0.8	0.3 to 0.8
$\frac{d \ln \mathrm{LWP}}{d \ln N_d}$	$\beta_{\ln \mathcal{L} - \ln N}$	-0.36 to -0.011	-0.36 to -0.011
$\frac{dC_{\mathrm{tot}}}{d \ln N_d}$	$\beta_{C - \ln N}$	0 to 0.1	0 to 0.1
effective cloud fraction for Twomey effect	c_N	0.19 to 0.29	0.20 to 0.29
effective cloud fraction for LWP adjustment	c_L	0.21 to 0.29	0.26 to 0.34
effective cloud fraction for cloud-fraction adjustment	c_C	0.59 to 1.07	0.61 to 0.96

*These terms represent $S_{\mathcal{L},N}$ and $S_{C,N}$ as defined in equations 19 and 21 of B20.

**B20's original assessment of $\partial R/\partial \ln \mathrm{LWP}$ and $\partial R/\partial C_{\mathrm{tot}}$ represents top-of-atmosphere net radiation. They assess the SW component of $\partial R/\partial \ln \mathrm{LWP}$ and $\partial R/\partial C_{\mathrm{tot}}$, then scale the values by 0.9 to account for an offsetting change in top-of-atmosphere longwave flux. In our analysis, we estimate the SW component of ERF_{aci}, so we do not apply the scaling factor of 0.9.

Table S3 Estimates of SW aerosol indirect effects and effective radiative forcing averaged over ocean between 55°S and 55°N. The values in the table are plotted in Fig. 3 and Fig. 5 in the main text, except for the values in the fifth column, which are included here to facilitate comparisons with other studies. In that column, R_{int} represents the radiative impacts of overall cloud-albedo anomalies ($R'_{\mathrm{int}} \equiv R'_{r_e} + R'_{\mathrm{LWP}} + R'_{\mathrm{res}}$), and $\mathrm{ERF}_{\mathrm{aci,res}}$ is the residual of the $\mathrm{ERF}_{\mathrm{aci}}$ decomposition. The first value in each table entry is the $\mathrm{MODIS}_{\mathrm{CLD}}$ estimate, and the second value is the $\mathrm{MODIS}_{\mathrm{CLD+PCL}}$ estimate. Uncertainties are 95% CIs.

Regressions against $\ln s$					
$\partial R_{r_e}/\partial \ln s$	$\partial R_{\mathrm{LWP}}/\partial \ln s$	$\partial R_{\mathrm{CF}}/\partial \ln s$*	$\partial R_{\mathrm{LWP+CF}}/\partial \ln s$	$\partial R_{\mathrm{int}}/\partial \ln s$**	$\partial R/\partial \ln s$
-1.24 ± 0.13 -1.28 ± 0.13	$+0.81 \pm 0.17$ $+0.32 \pm 0.24$	-2.33 ± 0.47 -1.55 ± 0.36	-1.53 ± 0.57 -1.22 ± 0.55	-0.52 ± 0.16 -1.15 ± 0.24	-2.86 ± 0.57 -2.70 ± 0.55
Regressions against $\ln \widetilde{N}_d$					
$\partial R_{r_e}/\partial \ln \widetilde{N}_d$	$\partial R_{\mathrm{LWP}}/\partial \ln \widetilde{N}_d$	$\partial R_{\mathrm{CF}}/\partial \ln \widetilde{N}_d$*	$\partial R_{\mathrm{LWP+CF}}/\partial \ln \widetilde{N}_d$	$\partial R_{\mathrm{int}}/\partial \ln \widetilde{N}_d$**	$\partial R/\partial \ln \widetilde{N}_d$
-4.38 ± 0.11 -4.54 ± 0.12	$+1.60 \pm 0.21$ $+0.77 \pm 0.31$	-3.99 ± 0.60 -2.46 ± 0.46	-2.39 ± 0.73 -1.68 ± 0.71	-3.04 ± 0.19 -4.37 ± 0.29	-7.03 ± 0.72 -6.83 ± 0.69
Components of SW $\mathrm{ERF}_{\mathrm{aci}}$					
$\mathrm{IRF}_{\mathrm{aci}}$	A_{LWP}	A_{CF}*	$A_{\mathrm{LWP}} + A_{\mathrm{CF}}$	$\mathrm{IRF}_{\mathrm{aci}} + A_{\mathrm{LWP}} + \mathrm{ERF}_{\mathrm{aci,res}}$**	$\mathrm{ERF}_{\mathrm{aci}}$
-0.77 ± 0.25 -0.79 ± 0.26	$+0.41 \pm 0.23$ $+0.08 \pm 0.18$	-1.42 ± 0.49 -0.88 ± 0.34	-1.02 ± 0.43 -0.80 ± 0.39	-0.44 ± 0.16 -0.86 ± 0.39	-1.86 ± 0.62 -1.74 ± 0.59

*This component represents aerosol-driven changes in the overall cloud amount with the normalized distribution of cloud albedo held fixed. Some studies refer to this component as the "extrinsic" component of aerosol indirect effects.

**This component represents aerosol-driven changes in the normalized distribution of cloud albedo with the overall cloud amount held fixed. Some studies refer to this component as the "intrinsic" component of aerosol indirect effects.

Supplementary Text

Validation of R' Decomposition

Our radiative decomposition method partitions R' into components associated with cloud-amount anomalies, r_e anomalies, LWP anomalies, and a residual:

$$R' = R'_{\mathrm{CF}} + R'_{r_e} + R'_{\mathrm{LWP}} + R'_{\mathrm{res}}.$$

We validate this decomposition using synthetic-data test cases performed with pixel data from the MODIS MYD06_L2 dataset collection 6.1 (Platnick et al., 2015). Each case uses pixels from a $1° \times 1°$ ocean grid box from the entire month of June 2013. Let $r_{e,j}$, LWP_j, and τ_j represent the retrieved cloud-droplet effective radius, liquid water path, and cloud visible optical thickness, respectively, for a pixel j containing a liquid cloud. For the test cases, we define the original cloud population as the set of all liquid-cloud pixels in the grid box with optical properties given by $r_{e,j}$, LWP_j, and τ_j. We then modify the cloud properties to create a second cloud population, denoted by $\tilde{r}_{e,j}$, $\widetilde{\mathrm{LWP}}_j$, and $\tilde{\tau}_j$, while holding the total number of liquid-cloud pixels constant. The difference in the monthly-mean grid-box-mean SW CRE between the two cloud populations, R', is then computed. We decompose R' separately using theoretical calculations and the radiative-kernel method, and we compare the estimates for validation.

The first step is to define the modified liquid-cloud population. We define the following relationships between the original and modified clouds:

$$\delta_{r_e,j} \equiv \tilde{r}_{e,j} - r_{e,j} = \chi_{r_e} r_{e,j},$$

$$\delta_{\mathrm{LWP},j} \equiv \widetilde{\mathrm{LWP}}_j - \mathrm{LWP}_j = \begin{cases} \chi_{\mathrm{LWP},1}\mathrm{LWP}_j, & r_{e,j} < 14\ \mu\mathrm{m} \\ \chi_{\mathrm{LWP},2}\mathrm{LWP}_j, & r_{e,j} \geq 14\ \mu\mathrm{m}. \end{cases}$$

where δ represents the difference between the original and modified cloud properties and χ_{r_e}, $\chi_{\mathrm{LWP},1}$, and $\chi_{\mathrm{LWP},2}$ are prescribed constants. A piecewise relationship for $\delta\mathrm{LWP}_j$ is chosen because precipitating and non-precipitating clouds can be approximately distinguished based on the clouds that have $r_e \geq 14\ \mu$m and $r_e < 14\ \mu$m, respectively (Freud and Rosenfeld, 2012; Suzuki et al., 2010). We prescribe separate relationships for precipitating and non-precipitating clouds to mimic the fact that they can have distinct responses to CCN anomalies. Calculations are performed with χ_{r_e}, $\chi_{\mathrm{LWP},1}$, and $\chi_{\mathrm{LWP},2}$ ranging from -0.1 to 0.1 in increments of 0.005 at three grid boxes corresponding to typical midlatitude, stratocumulus, and trade-cumulus conditions (Fig. S3a). Each combination of χ_{r_e}, $\chi_{\mathrm{LWP},1}$, $\chi_{\mathrm{LWP},2}$, and grid-box location is referred to as a test case.

We next estimate the difference in liquid-cloud SW CRE between the original and modified cloud populations for each test case under idealized conditions. Assuming that the ocean surface is black, that cloud droplets have a constant asymmetry factor of $g = 0.85$, and neglecting SW absorption by clouds and atmospheric gases, the top-of-atmosphere albedo above each liquid-cloud pixel, α_j, can be estimated using the two-stream radiative transfer approximation (Petty, 2006):

$$\alpha_j = \frac{(1-g)\tau_j}{1+(1-g)\tau_j}.$$

The cloud visible optical thickness τ is proportional to LWP/r_e in this cloud model, so the albedo difference between the original and modified cloud populations can be expressed as

$$\delta\alpha_j \equiv \tilde{\alpha}_j - \alpha_j = \delta\alpha_{\mathrm{LWP},j} + \delta\alpha_{r_e,j}$$

where

$$\delta\alpha_{\mathrm{LWP},j} = \frac{\delta\mathrm{LWP}_j}{\mathrm{LWP}_j}\frac{(1-g)\tau_j}{\left(1+(1-g)\tau_j\right)^2}$$

and

$$\delta\alpha_{r_e,j} = -\frac{\delta r_{e,j}}{r_{e,j}}\frac{(1-g)\tau_j}{\left(1+(1-g)\tau_j\right)^2}.$$

Here, $\delta\alpha_{\mathrm{LWP},j}$ and $\delta\alpha_{r_e,j}$ are the components of $\delta\alpha_j$ that are caused by $\delta\mathrm{LWP}_j$ and $\delta r_{e,j}$, respectively. We next average over all liquid-cloud pixels to determine the components of R' at the monthly-mean grid-box-mean scale:

$$R'_{\mathrm{LWP}} = \mathrm{SW}_{\downarrow} f_{\mathrm{liq}} \frac{1}{N}\sum_{j=1}^{N} \delta\alpha_{\mathrm{LWP},j},$$

$$R'_{r_e} = \mathrm{SW}_{\downarrow} f_{\mathrm{liq}} \frac{1}{N}\sum_{j=1}^{N} \delta\alpha_{r_e,j},$$

where $\mathrm{SW}_{\downarrow}$ is the monthly-mean insolation; N is the number of liquid-cloud pixels in the grid box; and $f_{\mathrm{liq}} \equiv N/N_{tot}$, where N_{tot} is the total number of pixels in the grid box. The liquid-cloud fraction is held constant in the test cases, so $R'_{\mathrm{CF}} = 0$.

We next decompose R' using the radiative kernel method. For consistency with the theoretical calculations, the kernel for this analysis is computed with a surface albedo of zero and with no SW absorption by water vapor or ozone. We then bin the liquid-cloud pixels into joint histograms partitioned by r_e and LWP. Let C_{rl} and $\tilde{C}_{rl}$ represent the joint histograms of the original and modified cloud populations, respectively. We define the cloud-fraction anomalies as $C'_{rl} = \tilde{C}_{rl} - C_{rl}$, and we estimate R'_{r_e}, R'_{LWP}, and R'_{res} with the kernel method.

This set of calculations produces estimates of R'_{r_e} for R'_{LWP} from two independent methods for each of the $\sim 2 \times 10^5$ test cases. The theoretical and kernel-based estimates approximately agree across all test cases, and the residual of the kernel

decomposition is almost always one order of magnitude smaller than R'_{r_e} and R'_{LWP} (Fig. S3). This verifies that the kernel method accurately decomposes R' into r_e-driven and LWP-driven components with a relatively small residual.

Assumptions about Cloud Vertical Structure

τ and LWP can be expressed as

$$\tau = \int_0^h \frac{3Q_e q_l(z)}{4\rho_l r_e(z)} dz$$

and

$$\mathrm{LWP} = \int_{z=0}^{h} q_l(z) dz,$$

where z is height above cloud base, h is cloud geometric thickness, $q_l(z)$ is the vertical profile of liquid water content, $r_e(z)$ is the vertical profile of cloud droplet effective radius, ρ_l is liquid-water density, and $Q_e \approx 2$ is the extinction efficiency at visible wavelengths. The MODIS observations can be used to directly infer τ and r_e near cloud top, but they do not constrain the other parameters in these equations. Thus, MODIS infers LWP indirectly by assuming vertical profiles of $q_l(z)$ and $r_e(z)$. Because τ is proportional to the integral of $q_l(z)/r_e(z)$, different profiles of $q_l(z)$ and $r_e(z)$ can be consistent with the observed value of τ. This means that the true LWP can differ from the MODIS estimate if the true profiles of $q_l(z)$ and $r_e(z)$ differ from the assumed profiles. This LWP bias can occur despite the fact that τ is well constrained by the observations.

We investigate the implications of assumptions about cloud vertical structure by considering three idealized cloud profiles. First, case VU assumes that $q_l(z)$ and $r_e(z)$ are vertically uniform inside the cloud. This assumption is made in the operational MODIS retrieval algorithm. Second, case AD assumes that $q_l(z)$ and $r_e(z)$ vary vertically according to the adiabatic cloud model (Brenguier et al., 2000). In this case, N_d is constant and $q_l(z)$ increases linearly with height. Third, case 2L assumes that the cloud has two vertically uniform layers following the assumptions in the radiative kernel calculations. The top layer has optical thickness $\tau_1 = 3$, LWP denoted by LWP_1, and effective radius $r_{e,1} = r_{e,\mathrm{top}}$, where $r_{e,\mathrm{top}}$ is the cloud droplet effective radius at cloud top. The bottom layer has optical thickness of $\tau_2 = \tau - \tau_1$, LWP denoted by LWP_2, and effective radius $r_{e,2} = m r_{e,\mathrm{top}} + b$, where τ is the total cloud optical thickness and m and b are constants.

For all three cases, τ, LWP, and $r_{e,\mathrm{top}}$ can be related to one another with analytic expressions. The VU and AD cases satisfy the following relations:

$$\text{VU case: } \tau = \frac{3Q_e \mathrm{LWP}_{\mathrm{VU}}}{4\rho_l r_{e,\mathrm{top}}}$$

$$\text{AD case: } \tau = \frac{9Q_e \mathrm{LWP}_{\mathrm{AD}}}{10\rho_l r_{e,\mathrm{top}}}$$

where LWP_{VU} and LWP_{AD} are the LWP values inferred from the VU and AD assumptions, respectively (Wood and Hartmann, 2006). The 2L case is represented by two cloud layers that each satisfy the VU relation:

$$\text{2L case: } \tau = \frac{3Q_e}{4\rho_l}\left(\frac{\text{LWP}_1}{r_{e,1}} + \frac{\text{LWP}_2}{r_{e,2}}\right)$$

For a given τ and $r_{e,\text{top}}$, the LWP inferred from these assumptions differ from one another by 17% or less.

We next examine how the assumptions about cloud vertical structure affect estimates of the R' components. Consider two liquid-cloud pixels in which τ and $r_{e,\text{top}}$ are known from MODIS observations. Differentiating the above equations leads to the following relations:

$$\text{VU case: } \delta \ln \tau \approx \delta \ln \text{LWP}_{\text{VU}} - \delta \ln r_{e,\text{top}}$$

$$\text{AD case: } \delta \ln \tau \approx \delta \ln \text{LWP}_{\text{AD}} - \delta \ln r_{e,\text{top}}$$

$$\text{2L case: } \delta \ln \tau \approx \left(\frac{\tau_1}{\tau_1+\tau_2}\delta \ln \text{LWP}_1 + \frac{\tau_2}{\tau_1+\tau_2}\delta \ln \text{LWP}_2\right) - \left(\frac{\tau_1}{\tau_1+\tau_2}\delta \ln r_{e,1} + \frac{\tau_2}{\tau_1+\tau_2}\delta \ln r_{e,2}\right)$$

where δ represents the difference between the two pixels. The first and second terms on the right side of these equations represent the δLWP-driven and $\delta r_{e,\text{top}}$-driven components of $\delta \ln \tau$, respectively. These components are identical for the VU and AD cases because LWP_{VU} is directly proportional to LWP_{AD}. The components of $\delta \ln \tau$ from the VU and AD cases are also similar to those from the 2L case. For instance, if typical values of $\tau = 10$ and $r_{e,\text{top}} = 14\ \mu$m are assumed and $\delta \ln \tau$ and $\delta \ln r_{e,\text{top}}$ are varied between 0 and 1, then the δLWP-driven and $\delta r_{e,\text{top}}$-driven components of $\delta \ln \tau$ differ by 2% or less between the three cases. This means that different common assumptions about cloud vertical structure will lead to similar estimates of R'_{r_e} and R'_{LWP}.

Estimating ERF_{aci} from the Method of Bellouin et al. (2020)

We compare our estimates of SW ERF_{aci} from liquid clouds with estimates from the assessment of the WCRP reported by Bellouin et al. (2020; hereafter B20). B20 assess the components of ERF_{aci} according to

$$\text{IRF}_{\text{aci}} = \frac{\partial R}{\partial \ln N_d}\frac{\partial \ln N_d}{\partial \ln \tau_a}\frac{\Delta \tau_a}{\tau_{a,\text{PD}}} c_N,$$

$$\text{A}_{\text{LWP}} = \frac{\partial R}{\partial \ln \text{LWP}}\frac{d \ln \text{LWP}}{d \ln N_d}\frac{\partial \ln N_d}{\partial \ln \tau_a}\frac{\Delta \tau_a}{\tau_{a,\text{PD}}} c_{\text{L}},$$

and

$$A_{CF} = \frac{\partial R}{\partial C_{tot}} \frac{dC_{tot}}{d \ln N_d} \frac{\partial \ln N_d}{\partial \ln \tau_a} \frac{\Delta \tau_a}{\tau_{a,PD}} c_C,$$

where τ_a is aerosol optical depth, "PD" represents present day, and Δ represents the difference between present day and preindustrial conditions. All terms in these equations are global averages, and c_N, c_L, and c_C are effective cloud fractions that account for spatial correlations between the other variables. We estimate the components of ERF_{aci} following the method of B20, but we modify the values so that they represent averages over our study domain rather than the entire globe. c_N, c_L, c_C, $\partial R / \partial \ln N_d$, and $\partial R / \partial \ln \mathrm{LWP}$ are computed following B20's method but restricting the calculation to ocean grid boxes between 55°S and 55°N. We use B20's estimates of $\partial R / \partial C_{tot}$, $\partial \ln N_d / \partial \ln \tau_a$, $d \ln \mathrm{LWP} / d \ln N_d$, and $dC_{tot} / d \ln N_d$ because they are assessed from studies that mostly investigate clouds in oceanic and coastal environments. One exception is the upper bound of $dC_{tot} / d \ln N_d$, which is assessed over the entire globe using GCM output. Finally, we scale B20's estimate of $\tau_{a,PD}$ by a factor of $\langle \tau_{a,PD} \rangle_{ocean} / \langle \tau_{a,PD} \rangle_{global}$, where $\langle \tau_{a,PD} \rangle_{ocean}$ is the average of $\tau_{a,PD}$ over ocean between 55°S and 55°N and $\langle \tau_{a,PD} \rangle_{global}$ is the average of $\tau_{a,PD}$ over the entire globe. Similarly, we scale B20's estimate of $\Delta \tau_a$ by $\langle \Delta \tau_a \rangle_{ocean} / \langle \Delta \tau_a \rangle_{global}$. These scaling factors are calculated with data from the Monitoring Atmospheric Composition and Climate Reanalysis (Benedetti et al., 2009) for consistency with B20. The original and modified values of all parameters are listed in Table S2.

Supplementary References

Bellouin, N., et al.: Bounding Global Aerosol Radiative Forcing of Climate Change. *Rev. Geophys.*, 1–45. https://doi.org/10.1029/2019rg000660, 2020.

Benedetti, A., et al.: Aerosol Analysis and Forecast in the European Centre for Medium-Range Weather Forecasts Integrated Forecast System: 2. Data Assimilation. *J. Geophys. Res. Atmos.*, 114, D13,205. https://doi.org/10.1029/2008JD011115, 2009.

Bennartz, R., and Rausch, J.: Global and Regional Estimates of Warm Cloud Droplet Number Concentration Based on 13 Years of AQUA-MODIS Observations, *Atmos. Chem. Phys.*, 17, 9815– 9836, https://doi.org/10.5194/acp-17-9815-2017, 2017.

Brenguier, J. L., et al.: Radiative Properties of Boundary Layer Clouds: Droplet Effective Radius Versus Number Concentration. *J. Atmos. Sci.*, *57*(6), 803–821. https://doi.org/10.1175/1520-0469(2000)057<0803:RPOBLC>2.0.CO;2, 2000.

Freud, E., and Rosenfeld, D.: Linear Relation Between Convective Cloud Drop Number Concentration and Depth for Rain Initiation. *J. Geophys. Res. Atmos.*, *117*(2), 1–14, https://doi.org/10.1029/2011JD016457, 2012.

Grosvenor, D. P., et al.: Remote Sensing of Droplet Number Concentration in Warm Clouds: A Review of the Current State of Knowledge and Perspectives. *Rev. Geophy.*, *56*(2), 409–453. https://doi.org/10.1029/2017RG000593, 2018.

Gryspeerdt, E., et al.: Surprising Similarities in Model and Observational Aerosol Radiative Forcing Estimates. *Atmos. Chem. Phys.*, *20*(1), 613–623. https://doi.org/10.5194/acp-20-613-2020, 2020.

Petty, G. W.: *A First Course in Atmospheric Radiation, Second Edition* Ch. 13 (Sundog Publishing), 2006.

Platnick, S., et al.: MODIS Atmosphere L2 Cloud Product (06_L2). NASA MODIS Adaptive Processing System, Goddard Space Flight Center, USA: https://dx.doi.org/10.5067/MODIS/MYD06_L2.061, 2015.

Suzuki, K., Nakajima, T. Y., and Stephens, G. L.: Particle Growth and Drop Collection Efficiency of Warm Clouds as Inferred from Joint CloudSat and MODIS Observations. *J. Atmos. Sci.*, *67*(9), 3019–3032. https://doi.org/10.1175/2010JAS3463.1, 2010.

Wilks, D. S.: “The Stippling Shows Statistically Significant Grid Points.” How Research Results are Routinely Overstated and Overinterpreted, and What to Do about It. *Bull. Am. Meteorol. Soc.*, *97*, 2263–2274, https://doi.org/10.1175/BAMS-D-15-00267.1, 2016.

Wood, R., and Hartmann, D. L.: Spatial Variability of Liquid Water Path in Marine Low Cloud: The Importance of Mesoscale Cellular Convection. *J. Clim.*, *19*(9), 1748–1764. https://doi.org/10.1175/JCLI3702.1, 2006.

Zhu, Y., Rosenfeld, D., and Li, Z.: Under What Conditions Can We Trust Retrieved Cloud Drop Concentrations in Broken Marine Stratocumulus? *J. Geophys. Res. Atmos.*, *123*(16), 8754–8767. https://doi.org/10.1029/2017JD028083, 2018.